Atomic-level view of inelastic deformation in a shock loaded molecular crystal

Eugenio Jaramillo,[1,*] Thomas D. Sewell,[1,†] and Alejandro Strachan[2,‡]
[1]*Theoretical Division, Los Alamos National Laboratory, Los Alamos, New Mexico 87545, USA*
[2]*School of Materials Engineering, Purdue University, West Lafayette, Indiana 47907, USA*
(Received 8 May 2007; revised manuscript received 13 June 2007; published 16 August 2007)

We use molecular dynamics to characterize the atomic-level mechanisms of plastic deformation in an organic molecular crystal under dynamical loading, namely, α-octahydro-1,3,5,7-tetranitro-1,3,5,7-tetrazocine shocked in the [100] direction. Plasticity for weak shocks is governed by dislocations with Burgers vectors $b=1/2\ \langle 101\rangle$ gliding on {101} planes. As the shock strength is increased, we observe a gradual transition to a regime dominated by nanoscale shear bands that does not exhibit a preferred crystallographic slip and where the material becomes locally amorphous.

DOI: 10.1103/PhysRevB.76.064112 PACS number(s): 81.40.−z, 62.20.Fe, 62.50.+p

I. INTRODUCTION

Plastic deformation in crystalline metals is governed by dislocations; their mobility and interactions with other defects control the mechanical response of these materials under most loading conditions.[1] Dislocations are line defects that glide on preferred planes (typically closely packed ones) and, in doing so, cause an atomic-scale amount of plastic strain. The displacement that an individual dislocation causes when it glides is quantified by its Burgers vector. Since the existence of dislocations was proposed independently in 1934 by Orowan,[2] Polanyi,[3] and Taylor,[4] experimental, theoretical, and computational works have advanced the field to maturity. Atomistic simulations played an invaluable role in this process, providing detailed information about core structures and dislocation mobility,[5–7] dislocations under dynamical loading,[8,9] and size-dependent phenomena.[10] We currently understand, both qualitatively and quantitatively for most crystalline metals, how macroscopic deformation is related to the properties of individual dislocations and the collective interactions among them. This constitutes the knowledge base for the development of predictive models for the mechanical behavior of metals that play an increasingly prominent role in materials science. A similar understanding for molecular materials is required and would impact a wide variety of fields ranging from pharmacy and biomaterials to energetic materials.[11] Despite such pressing needs, progress toward a molecular-level understanding of deformation in molecular materials has been slow. The presence of molecular and intramolecular degrees of freedom that couple with, and sometimes hinder, the intermolecular process of slip complicates descriptions of plasticity in molecular crystals.[12] Further challenges arise from the low-symmetry space groups typical of these materials and the need to account for the possibility of changes in molecular orientation and, often, molecular conformation in the description of crystal defects. Indeed, nearly all previous *in situ* studies of which we are aware have dealt with high-symmetry crystals and/or nearly rigid molecules, for example, hexamine,[13] naphthalene,[14] and buckminsterfullerene.[15] A notable exception is the work of Dick and Ritchie,[12] wherein constrained molecular mechanics simulations were used as a tool for interpreting macroscopic flyer plate measurements of the anisotropic detonation initiation sensitivity of the energetic material pentaerythritol tetranitrate.

In the present study, we use large-scale molecular dynamics (MD) simulations to characterize the fundamental mechanisms that govern the plastic response of the molecular crystal cyclic $[CH_2\text{-}N(NO_2)]_4$ (HMX) under dynamical loading. HMX is a high energy density material used in explosive and propellant formulations. It contains many of the complicated features mentioned above that distinguish most organic crystals from metals, namely, numerous internal degrees of freedom ($3N-3=81$ rovibrational modes per 28-atom molecule), conformational flexibility (multiple energetic minima with different molecular point groups),[16] and multiple low-symmetry crystal polymorphs.[17–19] In contrast to preceding reports for comparable materials,[12] in the present work we include all vibrational degrees of freedom except for C–H bond stretches. The outline of the remainder of the paper is as follows: computational methods are detailed in Sec. II, results and discussion are presented in Sec. III, and concluding remarks are given in Sec. IV. Animations of plasticity evolution for some trajectories are available as online supplementary material.[34]

II. COMPUTATIONAL APPROACH

A. Simulation details

The IUPAC name for HMX is octahydro-1,3,5,7-tetranitro-1,3,5,7-tetramine (see Fig. 1). The α polymorph studied here crystallizes into an orthorhombic structure with space group *Fdd*2 and eight molecules per unit cell, in a stacked arrangement (see inset to Fig. 2). Individual molecules have a C_2 rotation axis and are essentially basketlike with all four nitro groups ($-NO_2$) on the same side of the ring; the crystallographic asymmetric unit is one-half an HMX molecule.[19] The simulations were performed using the unreactive flexible-molecule force field for HMX due to Smith and Bharadwaj,[20] which has been used in several preceding studies of HMX crystal and liquid properties.[21–24] All C-H bonds were constrained to their equilibrium values using the SHAKE algorithm[25] to improve the description of the specific heat of the material in these nonequilibrium simulations.

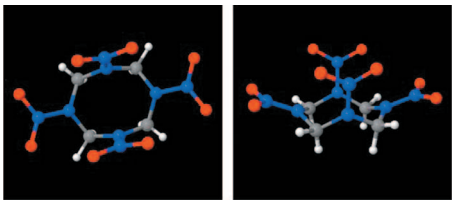

FIG. 1. (Color) Two views of the molecular structure of HMX. Gray, carbon; blue, nitrogen; red, oxygen; and white, hydrogen. The geometry shown corresponds to the α polymorph.

B. Initial conditions

Shockwaves were generated by driving the thermalized target material toward a piston whose atomic positions were held fixed during the duration of the simulation; this setup corresponds to a sustained shock. The target material contained 245 760 molecules in a $120\times8\times32$ arrangement of the unit cell, with initial dimensions of $185.8\times19.3\times19.5$ nm^3. Initial conditions were obtained by first performing 12 ps of isothermal-isochoric (*NVT*) equilibration for the target material, with cell dimensions corresponding to 300 K, atmospheric pressure, and three-dimensional periodic boundary conditions. The fixed piston was created by copying a $2\times8\times32$ unit from the thermalized supercell and replicating it, leaving a 2.7 nm gap between it and the target; a large gap was introduced at the other end of the simulation cell. This configuration containing the fixed piston and target was further equilibrated under *NVT* conditions for an additional 8 ps. The initial condition for a shock simulation was then obtained by adding the particle velocity $-\mathbf{u}_p$ on top of the thermal velocities of all atoms in the target. The process of shock propagation was simulated using constant volume and energy MD (*NVE* ensemble) until past the point of maximum compression in the shock wave.

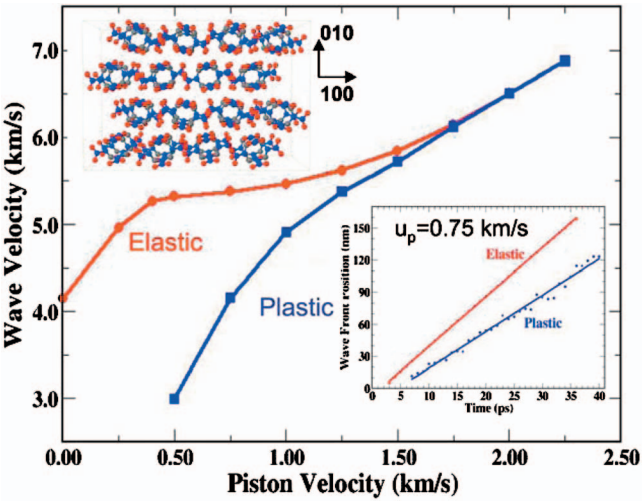

FIG. 2. (Color) Shock Hugoniot locus in the (u_s-u_p) plane for α-HMX shocked in the [100] direction. Upper inset: α-HMX crystal structure. Lower inset: representative position versus time plots for elastic and plastic waves for u_p=0.75 km/s, from which the corresponding velocities were obtained.

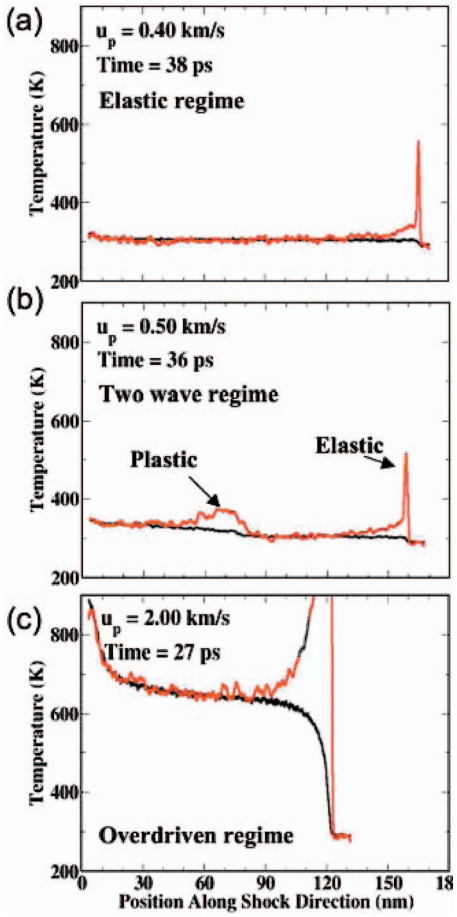

FIG. 3. (Color) Snapshots of intermolecular and intramolecular temperatures (red and black, respectively) plotted versus distance along the shock direction. The snapshots were taken close to points of maximum compression, for shocks propagating from left to right: (a) shock strength below the Hugoniot elastic limit, (b) shock strength within the elastic-plastic region, and (c) overdriven shock.

C. Trajectory integration

We used the velocity Verlet algorithm with a fixed time step of 0.4 fs to integrate the equations of motion; this was sufficient to obtain good energy conservation in the microcanonical (*NVE*) statistical ensemble simulations. Nonbonded repulsive and dispersion interactions, including unscaled 1–4 and lower order intramolecular nonbonded terms, were shifted smoothly to zero at a cutoff distance of 10.0 Å. The simulations were performed using a version of the LAMMPS (Ref. 26) molecular dynamics code modified to accommodate the Smith force field and shock wave boundary conditions. The particle-particle particle mesh (PPPM) algorithm included in LAMMPS was used to solve the electrostatic component of the problem.

III. SIMULATION ANALYSIS

A. Temperature

Inter- and intramolecular temperatures were obtained by separating relative translational and rovibrational velocity

contributions to the kinetic energy, respectively: $\mathbf{K}_{\text{tot}}=\mathbf{K}_{\text{trans}}+\mathbf{K}_{\text{rot-vib}}$. We used the weighting scheme due to Strachan and Holian[27] to obtain average, spatially localized temperatures. Let u_j denote the velocity of atom j, and $U_i=(1/M_i)\Sigma_j^{N_i^{at}} m_j u_j$ the center-of-mass (c.m.) velocity of molecule i. (M_i is the total mass of the molecule, the sum runs over all N_i^{at} atoms (j) in molecule i, and m_j is the mass of atom j.) In order to define intermolecular temperature, the local molecular velocity $\langle U\rangle_i$ around molecule i is defined in terms of its own c.m. velocity and those of its neighbors (j) at distance $r_{ij}=|r_i-r_j|$, modulated by a monotonically decreasing local weight function $w(r_{ij})$:

$$\langle U\rangle_i=\frac{\sum_j w(r_{ij})U_j}{\sum_j w(r_{ij})}; \tag{1}$$

then, the local intermolecular temperature T_i is given by

$$\frac{3}{2}k\langle T\rangle_i^{inter}=\frac{\frac{1}{2}\sum_j M_j w(r_{ij})|U_j-\langle U\rangle_i|^2}{\sum_j w(r_{ij})}, \tag{2}$$

where k is Boltzmann's constant. The intramolecular or vibrational temperature of each molecule is defined in terms of its kinetic energy measured in the c.m. frame:

$$\frac{3}{2}kN_i^{at}T_i^{intra}=\frac{1}{2}\sum_{j=1}^{N_i^{at}} m_j(u_j-u_i^{c.m.})^2, \tag{3}$$

and the average local vibrational temperature in the neighborhood of molecule i is

$$\langle T\rangle_i^{intra}=\frac{\sum_j w(r_{ij})T_j}{\sum_j w(r_{ij})}. \tag{4}$$

Local temperatures as defined above were further averaged through the thickness of the simulation cell for thin slices perpendicular to the shock direction, yielding temperature as a function of position along the shock axis. The latter averaging was not done for spatially resolved temperature maps so as to more accurately reflect the fluctuations in temperature associated with plastic deformation.

B. Plastic deformation

In order to characterize at the molecular level the fundamental processes that govern plastic deformation, we analyzed relative displacements of nearest-neighbor molecular centers of mass: $\Delta_{ij}(t)=r_{ij}(0)-r_{ij}(t)$, where i and j are pairs of molecules that are nearest neighbors at time $t=0$, and $r_{ij}(0)$ and $r_{ij}(t)$ represent the vector separating them at time $t=0$ (the reference state before any deformation has occurred) and the analysis time (t), respectively. $\Delta_{ij}(t)$ for all pairs of initial nearest neighbors provides a complete molecular picture of the elastic and plastic deformations of the material.

Once Δ_{ij} is calculated for a pair of molecules, the displacement is classified into

(i) elastic if $|\Delta_{ij}|<2$ Å,

(ii) $b=1/2\langle 101\rangle$ dislocation-based if Δ_{ij} is within 1.5 Å of either (7,0,3) Å or (7,0,−3) Å, or

(iii) nanoshear band if it does not fall into either category.

The type of deformation is recorded for each molecule and this process is repeated for all pairs of nearest-neighbor molecules. Ultimately, a molecule is defined as having undergone

(i) dislocation-based plastic deformation if it has undergone more than four dislocation-type transitions with respect to its neighbors,

(ii) elastic or no deformation if the condition for dislocation-based plasticity is not met and it has undergone elastic deformation with respect to more than four neighbors, or

(iii) nanoshear band deformation if neither of the two preceding conditions has been met.

The results of the mechanistic analysis are not highly sensitive to the fine details of these definitions.

C. Conformational changes in tetrazocine ring

The analysis of ring conformations was based on the sequential ordering of relative signs of the eight ring dihedral angles. In particular, the sign of each C-N-C-N and N-C-N-C dihedral angle in a molecule was obtained, and the ordered sequence was compared to those determined for the various possible conformations of HMX (see Ref. 20). There are a limited number of possibilities for an eight-membered ring, for example, the signs of consecutive dihedrals for the α conformer of HMX alternate $(+-+-+-+-)$ while for the boat-boat conformer they appear in alternating pairs $(++--++--)$. Other ring conformers correspond to comparably well-defined sequences of dihedral angle signs, and these were found to be clearly distinguishable in most cases. Although an analysis that involves all transitions between one or another conformation is possible, for the purposes of this paper, we focus on changes "away" from the initial α ring conformation.

IV. RESULTS AND DISCUSSION

Our interest is in the thermomechanical response of a sample specimen of α-HMX when impacted by an infinitely massive flyer plate with prescribed piston velocities u_p along the [100] direction of the orthorhombic crystal. We considered u_p between 0.25 and 2.25 km/s.

A. Shock Hugoniot locus

Figure 2 depicts the predicted shock Hugoniot locus in the shock velocity/piston velocity plane.[28] For $u_p\leqslant 0.40$ km/s, the uniaxial compression (with pressure along the shock direction $P_{xx}=\rho_0 u_s p_p\leqslant 3.8$ GPa) is insufficient to trigger plastic deformation; here, ρ_0 is the initial density and u_s is the shock velocity. This elastic regime is characterized by a

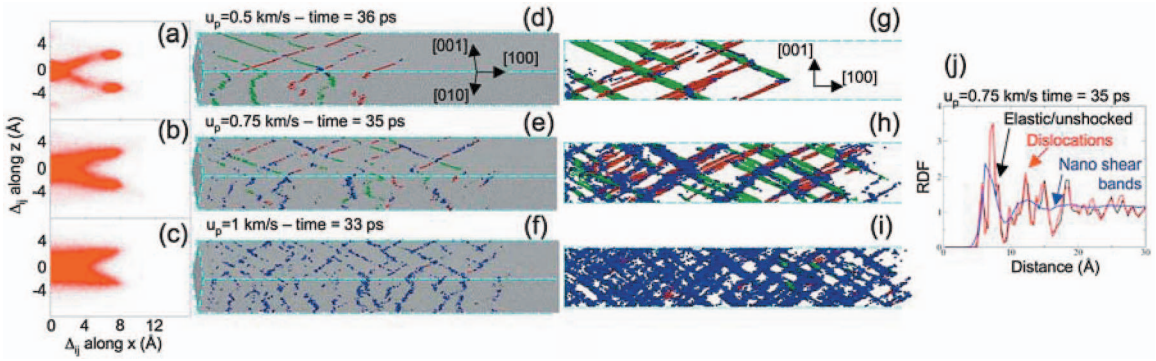

FIG. 4. (Color) Depictions of plasticity in HMX for shock states spanning the two-wave region. Results are for individual snapshots taken near maximum compressions. (a)–(c) Distributions of local molecular displacements, $\Delta_{ij}(t)$, projected onto the (010) plane. (d)–(f) Dislocations and shear bands at the "surface" of the simulation cell. Red and green correspond to $b=1/2[101]$ and $1/2[10\bar{1}]$ dislocations, respectively; blue corresponds to shear bandlike deformation. (g)–(i) As in (d)–(f) except that the view is through the simulation cell in a direction normal to the (010) plane. (j) Radial distribution functions for elastically compressed molecules (black) and those that have undergone dislocation slip (red) or nanoscale shear-band deformation (blue). The shock strength is $u_p=0.75$ km/s.

single wave with shock velocity linearly proportional to particle velocity; as u_p tends to zero, the wave speed tends to the longitudinal sound speed c_0^l.[29]

For $u_p=0.50$ km/s ($P_{xx}=4.7$ GPa), inelastic deformation nucleates in the shocked material to release the uniaxial compression toward a hydrostatic state (i.e., equal stress in all directions); a wave of plastic deformation results that moves at a slower speed than the elastic wave. Thus, the Hugoniot elastic limit (HEL), a measure of the strength of the material defined as the minimum shock strength necessary to initiate plastic deformation, corresponds to piston velocities between 0.4 and 0.5 km/s. (In fact, this interval defines an upper limit to the HEL due to the finite time and space scales accessible in the simulations.) The two-wave elastic-plastic structure exists for $0.50 \leqslant u_p \leqslant 1.50$ km/s ($4.7 \leqslant P_{xx} \leqslant 23.2$ GPa). Within this approximate interval, larger values of u_p lead to increases in the plastic wave speed, while the elastic wave speed remains nearly constant, thereby reducing the rate of growth of the elastic precursor region. The plastic wave ultimately overtakes the elastic one at $u_p \sim 1.50$ km/s ($P_{xx}=23.2$ GPa), resulting in a single, overdriven wave in which inelastic deformation nucleates right behind the shock.

B. Temperature

The arrival of both the elastic and plastic waves causes temperature rise in the material, as shown in Fig. 3. The wide range of vibrational frequencies in molecular crystals leads to a variety of time scales associated with temperature rise, leading to nonequilibrium states for considerable distances (times) behind the shock front, even for shock pressures below the HEL. The translational energy of the shock couples most efficiently to the low-frequency lattice degrees of freedom. The intermolecular temperature has a very short rise time and overshoots its final value since the few molecular degrees of freedom—three per molecule—initially have to accommodate nearly all the shock energy. (The overshoot in Fig. 3 is also due in part to the very narrow shock front that makes calculation of local temperatures difficult.) This excitation energy relaxes among the higher-frequency intramolecular modes, causing the vibrational temperature to increase until the two measures of temperature reach the same value and the system is in local thermal equilibrium. The largely unexplored dynamical interplay among the modes in the system arises due to the significant range of vibronic frequencies in HMX and their relative coupling strengths to the low-frequency lattice modes; such behavior does not exist in atomic materials.

C. Mechanisms of plastic deformation

We use the methodology described in Sec. III B to characterize the mechanisms of plastic deformation. Figures

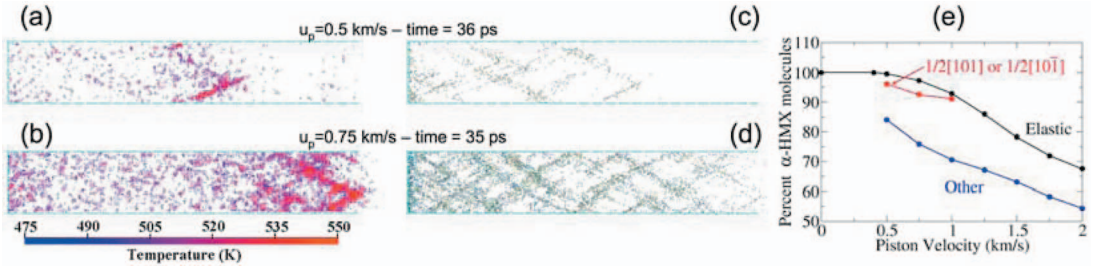

FIG. 5. (Color) (a) and (b) Spatial distributions of intermolecular temperature in α-HMX for two shock strengths in the elastic-plastic region. (c) and (d) As in (a) and (b) except that the plots depict those molecules that have undergone conformational change. (e) Percentage versus shock strength (piston velocity) of molecules that remain in the α conformation at the end of the simulations. Black, red, and blue correspond to molecules in regions of elastic compression, dislocation slip, and shear bandlike local plastic deformation, respectively.

4(a)–4(c) (left-hand column) show the distribution of the relative molecular displacement $\Delta_{ij}(t)$ in the (010) plane at the time of maximum compression for three piston velocities. For u_p=0.5 km/s, the molecular displacements cluster predominantly around three areas: zero, (7.5,0,−3) Å, and (7.5,0,3) Å. The first of these corresponds to unshocked or elastically deformed material, while the latter two correspond to $1/2[10\bar{1}]$ and $1/2[101]$ crystallographic directions and indicate the Burgers vector of dislocations gliding on (101) and $(10\bar{1})$ crystal planes. We also observe [001] and $[00\bar{1}]$ slip, to a lesser extent and at longer times, resulting from the intersection of the two primary slip events, leading to the addition of their Burgers vectors. All Burgers vectors observed correspond to translational symmetries of α-HMX and, consequently, full dislocations are responsible for plastic deformation. As u_p is increased to 0.75 km/s, a significant number of slip events fall outside the crystallographically well-defined regions that dominate deformation for the weaker shock. For even higher piston velocities, the relative molecular displacements do not cluster around any specific crystallographic direction.

In order to provide a more complete picture of the inelastic response of HMX, we also show in Fig. 4 snapshots from our MD simulations where each molecule is colored according to its relative molecular displacement. Unshocked and elastically deformed molecules are depicted as gray spheres (second column) or not at all (third column); green and red spheres represent $1/2[10\bar{1}]$ and $1/2[101]$ slip, respectively. For shocks just above the HEL, the first plastic event is the nucleation of a dislocation loop encircling $1/2[10\bar{1}]$ slip behind the shock front; $1/2[101]$ loops are nucleated subsequently. For these relatively weak shocks, dislocations are the main carriers of plasticity; as shown in Fig. 4 for u_p =0.5 km/s, deformation is confined to molecularly thin planes. Screw segments undergo frequent cross slip, leading to wavy traces on the (001) face, whereas the inability of the edge segments to cross slip leads to straight traces on the (010) face. The intersection of the active slip planes and the (010) plane forms angles of ±61.27° relative to the shock direction. As the shock strength is increased, there is a gradual transition away from dislocation-based plasticity dominated by crystallographic slip toward a mechanism in which deformation is clustered in nanosized shear bands (blue spheres in Fig. 4 denote molecules that have undergone significant relative displacement with their neighbors but do not fall in either $1/2[10\bar{1}]$ or $1/2[101]$). These nanoshear bands are several unit cells in thickness and, as in the dislocation-based case, plastic deformation results from the cumulative effect of many relatively small displacements between large numbers of neighboring molecules [see Fig. 4(a)–4(c)]. Another important difference between the two regimes is that the nanoshear bands make an angle very close to 45° relative to the loading direction, corresponding to the maximum resolved shear stress, whereas the crystallography of α-HMX determines the active slip planes in the dislocation-dominated regime. Finally, we show in Fig. 4(j) local radial distribution functions corresponding to molecular centers of mass for elastically compressed molecules (black), those that have undergone dislocation slip (red), and those in the shear bandlike regions (blue). The analysis was performed for the case u_p=0.75 km/s, for which both mechanisms of plastic deformation coexist. As expected, dislocation slip leads to essentially perfect recovery of the translational symmetry of the crystal, whereas the shear bands lead to an amorphous structure in which long-range order is erased. This mechanism exhibits signatures of macroscopic shear bands,[30] albeit on a much smaller spatial scale.

So far, our analysis of deformation has focused on the molecular centers of mass. While this would exhaust all possibilities in atomic materials, molecular ones exhibit richer phenomena due to the irregular shapes of the molecules and the large number of intramolecular degrees of freedom that are excited during the deformation process. Plastic deformation results in localization of the shock energy in narrow bands, which leads, in turn, to significant local heating. Local temperatures in shear and slip bands can be as much as 30% higher than in the elastically compressed regions at corresponding distances behind the shock (left-hand column in Fig. 5). The hot regions in the temperature maps clearly correlate with the regions of plastic activity in Fig. 4, and are of particular interest due to local thermodynamic and kinetic changes that might occur within them (e.g., phase changes, chemical reaction), with the potential for concomitant changes in important properties such as material strength, chemical stability, or rate of biological uptake.

D. Ring conformational changes

Molecules that undergo changes in conformation of the eight-membered ring in HMX during shock loading are shown in the center column of Fig. 5. Such intramolecular transitions only appear for shock strengths above the HEL, demonstrating a strong correlation between plastic deformation and intramolecular changes. While molecules that do change conformation correlate strongly to plasticity events (and to increases in local temperature), those involved in $1/2[10\bar{1}]$ or $1/2[101]$ slip events are only slightly more likely to exhibit conformational changes than those in simple elastically compressed regions [Fig. 5(e)]. Thus, despite the complex molecular shape and packing in α-HMX, the motion of dislocations leaves the crystal essentially unchanged with minimal defect concentrations in their wake; molecules involved in plasticity maintain, or recover, their starting point-group symmetry and orientation. On the other hand, molecules involved in nanoshear band plasticity have a significantly higher probability to exhibit internal changes.

V. SUMMARY AND CONCLUSIONS

Our atomistic simulations provide a dynamic, molecular-level *in situ* characterization of the complex phenomena that govern the deformation of molecular crystals. We observe a gradual transition between a regime governed by dislocations, where the structural properties of the original crystal (both inter- and intramolecular characteristics) are maintained, and one dominated by nanoscale shear bands, where

the material is locally amorphized and intramolecular conformational changes are common. The nanoshear bands characterized in our simulations exhibit some properties of macroscopic shear bands, most importantly their amorphous character, but also some characteristics of dislocation-based plasticity: each molecule undergoes small displacement with respect to its neighbors.

The number of studies required to obtain a complete understanding of the thermomechanical response of molecularly complex crystals such as HMX is obviously enormous and the present work represents an important first step toward that goal. Careful consideration of atomic-scale computational results such as those provided here, interpreted with the aid of systematic experiments and continuum theoretical analyses,[31–33] will accelerate progress toward obtaining a credible, predictive understanding for these kinds of materials.

ACKNOWLEDGMENTS

Los Alamos National Laboratory is operated by Los Alamos National Security (LANS), LLC for the U.S. Department of Energy and National Nuclear Safety Administration. The authors thank M. Cawkwell, J. Dick, B. Holian, D. Hooks, R. Menikoff, S. Shaw, and V. Levitas for useful discussions.

*Present address: Department of Biology and Chemistry, Texas A&M International University, Laredo, TX 78041.
†sewell@lanl.gov
‡strachan@purdue.edu

[1] J. P. Hirth and J. Lothe, *Theory of Dislocations*, 2nd ed. (Wiley, New York, 1982).
[2] E. Orowan, Z. Phys. **89**, 605 (1934).
[3] M. Polanyi, Z. Phys. **89**, 660 (1934).
[4] G. I. Taylor, Proc. R. Soc. London, Ser. A **145**, 362 (1934).
[5] M. S. Duesbery and V. Vitek, Acta Mater. **46**, 1481 (1998).
[6] S. Ismail-Beigi and T. A. Arias, Phys. Rev. Lett. **84**, 1499 (2000).
[7] M. J. Cawkwell, D. Nguyen-Manh, C. Woodward, D. G. Pettifor, and V. Vitek, Science **309**, 1059 (2005).
[8] B. L. Holian and P. S. Lomdahl, Science **280**, 2085 (1998).
[9] E. M. Bringa, A. Caro, Y. Wang, M. Victoria, J. M. McNaney, B. A. Remington, R. F. Smith, B. R. Torralva, and H. Van Swygenhoven, Science **309**, 1838 (2005).
[10] J. Schiøtz and K. Jacobsen, Science **301**, 1357 (2003).
[11] R. W. Armstrong and W. L. Elban, in *Dislocations in Solids*, edited by J. P. Firth and F. R. N. Nabarro (Elsevier, Amsterdam, 2004), Vol. 12, Chap. 69.
[12] J. J. Dick and J. P. Ritchie, J. Appl. Phys. **76**, 2726 (1994).
[13] J. di Persio and B. Escaig, Phys. Status Solidi A **40**, 393 (1977).
[14] N. Ide, I. Okada, and K. Kojima, J. Phys.: Condens. Matter **5**, 3151 (1993).
[15] H. Hayashi, S. Tamaki, N. Ide, I. Okada, and K. Kojima, Jpn. J. Appl. Phys., Part 1 **41**, 6486 (2002).
[16] H. V. Brand, R. L. Rabie, D. J. Funk, I. Diaz-Acosta, P. Pulay, and T. K. Lippert, J. Phys. Chem. B **106**, 10594 (2002).
[17] C. S. Choi and H. P. Boutin, Acta Crystallogr., Sect. B: Struct. Crystallogr. Cryst. Chem. **26**, 1235 (1970).
[18] R. E. Cobbledick and R. W. H. Small, Acta Crystallogr., Sect. B: Struct. Crystallogr. Cryst. Chem. **30**, 1918 (1974).
[19] H. H. Cady, A. C. Larson, and D. T. Cromer, Acta Crystallogr. **16**, 617 (1963). Note that the "y" fractional coordinate for atom N_1 in Table II should have a negative sign.
[20] G. D. Smith and R. K. Bharadwaj, J. Phys. Chem. B **103**, 3570 (1999).
[21] D. Bedrov, C. Ayyagari, G. D. Smith, T. D. Sewell, and J. M. Zaug, J. Comput.-Aided Mol. Des. **8**, 77 (2000).
[22] D. Bedrov, G. D. Smith, and T. D. Sewell, Chem. Phys. Lett. **324**, 64 (2000).
[23] D. Bedrov, G. D. Smith, and T. D. Sewell, J. Chem. Phys. **112**, 7203 (2000).
[24] T. D. Sewell, R. Menikoff, D. Bedrov, and G. D. Smith, J. Chem. Phys. **119**, 7417 (2003).
[25] M. P. Allen and D. T. Tildesley, *Computer Simulation of Liquids* (Oxford, New York, 1987).
[26] S. J. Plimpton, J. Comput. Phys. **117**, 1 (1995); http://lammps.sandia.gov
[27] A. Strachan and B. L. Holian, Phys. Rev. Lett. **94**, 014301 (2005).
[28] That is, the locus of final states accessible via various degrees of shockwave loading for a given material in specified initial state.
[29] The value $c_0^l \sim 4.1$ km/s predicted here is significantly larger than the quasilongitudinal sound speed of 3.17 km/s reported for β-HMX along the (010) direction based on an ultrasonic measurement in Ref. 31; this is generally, although not quantitatively, consistent with the ratio of calculated elastic coefficients $C_{11}^{\alpha}/C_{22}^{\beta}=30.6$ GPa/23.9 GPa=1.28 (Ref. 24). Note also that the measured elastic tensor for β-HMX is still rather uncertain (Ref. 31).
[30] P. R. Guduru, A. J. Rosakis, and G. Ravichandran, Mech. Mater. **33**, 371 (2001).
[31] L. L. Stevens and C. J. Eckhardt, J. Chem. Phys. **122**, 174701 (2005).
[32] J. J. Dick, D. E. Hooks, R. Menikoff, and A. R. Martinez, J. Appl. Phys. **96**, 374 (2004).
[33] R. Menikoff, J. J. Dick, and D. E. Hooks, J. Appl. Phys. **97**, 023529 (2005).
[34] See EPAPS Document No. E-PRBMDO-76-062730 for animations of plasticity evolution for some trajectories. For more information on EPAPS, see http://www.aip.org/pubservs/epaps.html.